Next Materials 10 (2026) 101484

Contents lists available at ScienceDirect

Next Materials

journal homepage: www.sciencedirect.com/journal/next-materials

Research article

Highly efficient double halide perovskite for solar cell devices with DFT and SCAPS 1D analysis

Md. Mehedi Hasan [a,*], Abdul Khaleque [a], M.A. Rayhan [b], M. Islam [c], S. Mahmud [c], Ashraful Hossain Howlader [d]

[a] Department of Electrical & Electronic Engineering, Rajshahi University of Engineering & Technology, Rajshahi 6204, Bangladesh
[b] Department of Arts and Sciences, Bangladesh Army University of Science and Technology, Saidpur 5310, Nilphamari, Bangladesh
[c] Department of Electrical and Electronic Engineering, Jatiya Kabi Kazi Nazrul Islam University (JKKNIU), Mymensingh 2224, Bangladesh
[d] School of Photovoltaic and Renewable Energy Engineering, UNSW Sydney, Sydney, NSW 2033, Australia

ARTICLE INFO

Keywords:
Double halide perovskite
Density functional theory
Power conversion efficiency
Band alignment

ABSTRACT

Advancing sustainable photovoltaic technologies depends greatly on the development of high-performance perovskite solar cells (PSCs), and new materials continue to provide promising opportunities for improving device efficiency. This research investigates the double perovskite compound Cs_2TlRhI_6 as a potential light-harvesting material through first-principles calculations and device-level simulations. The material has a direct bandgap of 1.12 eV, a refractive index of about 3.1, low reflectivity (below 30%), and strong absorption in the visible range, all of which support its potential for photovoltaic applications. Furthermore, implementing our absorber in an optimized device structure, employing Cu_2O as the HTL and IGZO as the ETL, achieves a PCE of 25.78%, with a J_{SC} of 40.53 mA/cm^2, a V_{OC} of 0.79 V, and a FF of 80.40%. Temperature analysis indicates a slight reduction in performance at high temperatures, revealing good thermal stability of the device. This work opens up Cs_2TlRhI_6 as a promising and structurally stable material for future PSCs.

1. Introduction

The rapid progress in solar energy technologies has inspired great interest in PSCs [1]. Their efficiency has increased from 3.8% to 25.7% over the past decade [2,3]. This remarkable improvement is attributed to their excellent optoelectronic properties, such as long charge carrier diffusion lengths, high absorption coefficients, and tunable bandgaps [4–6]. The discovery of perovskites was first reported in 1839, when Gustav Rose identified the mineral and named it in honor of the Russian mineralogist Lev Perovski. These compounds typically adopt the ABX_3 perovskite structure, where 'A' denotes a monovalent cation such as methylammonium ($CH_3NH_3^+$), formamidinium ($NH_2CHNH_2^+$), or cesium (Cs^+); 'X' refers to a halide species, including chloride, fluoride, or iodide [7,8] and 'B' refers to a cation in the +2 oxidation state such as lead (Pb^{2+}), Sn and Ge [9] but the major hurdle in developing Sn-based SCs is their tendency to oxidize. To address these challenges double perovskite structures in $A_2BB'X_6$ format as Cs_2AgBiX_6, Cs_2TlRhX_6 etc. have gained attention [10,11]. These materials exhibit enhanced stability and suitable band gaps. A well accepted approach relies on the use of a mono and trivalent cation scheme to fabricate double PSCs, including $(MA)_2AgBiBr_6$, $Cs_2AgBiCl_6$, and $Cs_2AgBi_{0.75}Sb_{0.25}Br_6$ [12–14]. Moreover, silver (Ag^+) and bismuth (Bi^{3+}) in this compound also provide a better prospect for its practical use [13]. Recently, Toki et al. (2024) theoretically optimized a lead-free ITO/WS_2/$Cs_3Bi_2I_9$/Cu_2O/Ni PSC, achieving a PCE of 18.36% with enhanced environmental stability [15]. Furthermore, $Cs_2AgBiBr_6$ and Cs_2BiAgI_6 have attracted interest as stable double perovskites, with Density Functional Theory (DFT) and device simulations (using SCAPS-1D and WxAMPS) predicting up to 21.59% efficiency based on their favorable structural and optoelectronic properties [11]. In 2023, Hossain et al. conducted a combined DFT and SCAPS-1D analysis on $CsPbBr_3$-based all-inorganic PSCs, achieving a maximum PCE of 13.86% for the TiO_2/CFTS charge transport configuration, highlighting the crucial role of interface and transport layer optimization in enhancing device performance [16]. Sabbah et al. attained 26.3% efficiency in hydrogenated lead-free $Cs_2AgBiBr_6$ double PSCs through SCAPS-1D simulations and structural modifications [17]. Furthermore, in 2024, Lunge et al. proposed double perovskite solar cells based on $Cs_2AuBiCl_6$ with optimized charge-transport layers, achieving an efficiency of 21.16% [18]. In high-efficiency solar cells, perovskite materials usually have bandgaps between 1.48 eV and 1.62 eV [19]. Unlike typical perovskite materials, halide double perovskites (HDPs)

* Corresponding author.
E-mail address: mehedihasan.ruet.eee@gmail.com (M.M. Hasan).

https://doi.org/10.1016/j.nxmate.2025.101484
Received 19 September 2025; Received in revised form 16 November 2025; Accepted 26 November 2025
Available online 8 December 2025

usually have wider bandgaps, often greater than 2 eV, particularly those that include chloride and bromide anions [20]. For example, Slavney et al. (2018) studied Cs_2AgTlX_6 compounds (where X = Cl, Br) with narrower bandgaps. Their results showed strong agreement between theoretical predictions (1.91 eV and 0.8 eV) and experimental measurements (1.96 eV and 0.95 eV) [21]. Recently, in 2023, Amin et al. studied Cs_2TlRhX_6 (X = Cl, Br, I) using first-principle methods by TB-mBJ potential, discovering the bandgaps of 1.29 eV to 1.55 eV, which is applicable to solar energy harvesting [10]. Despite substantial advancements in designing high efficiency PSCs, several research gaps remain. Many studies still over rely on DFT-based optoelectronic analyses without incorporating device level simulations. In addition, critical environmental factors such as defect densities, series and shunt resistances, and temperature effects are often overlooked, even though they can significantly influence device performance.

In this article, the optoelectronic properties of Cs_2TlRhI_6 are examined using DFT with the HSE06 hybrid functional within the CASTEP framework. The absorber material exhibits 1.12 eV of direct bandgap, a strong absorption coefficient of 6×10^4 cm^{-1} in the visible range, and low reflectivity. Furthermore, when integrated into a photovoltaic device using SCAPS-1D with Cu_2O as the HTL and IGZO as the ETL, the system demonstrates excellent performance. It gains an efficiency of 25.78%, with an open circuit voltage (V_{OC}) of 0.79 V, a short circuit current density (J_{SC}) of 40.53 mA/cm^2, and a fill factor (FF) of 80.40%. Temperature analysis shows minor efficiency losses at higher temperatures, confirming the device's good thermal stability. Defect analysis indicates negligible impact from HTL and ETL defects, whereas higher defect densities in the absorber material significantly reduce performance. Resistance studies further reveal that increased series resistance degrades efficiency, while optimized shunt resistance suppresses leakage and ensures stable operation.

2. Methodology

2.1. CASTEP

The present work explores the optoelectronic behavior of the HDP compound $CsTlRhI_6$ via first-principles density functional theory [22]. Simulations were performed using the CASTEP module implemented in the *Material Studio* package [23], with pseudopotential selection prioritized for accurate structural and electronic optimization of semiconductors [24]. For structural optimization, the BFGS algorithm was used with a plane-wave cutoff of 500 eV, an energy convergence criterion of 5×10^{-6} eV/atom, and a $6 \times 6 \times 6$ k-point mesh. The relaxation was further constrained by a stress tolerance of 0.02 GPa together with a maximum force limit of 0.01 eV/Å, while the atomic displacement threshold was set to 5×10^{-4} Å. Since GGA generally underestimates semiconductor band gaps, the hybrid HSE06 functional [25] was employed to achieve more reliable band gap values.

2.2. Fundamental theory and device layout

SCAPS-1D software will be used to assess the proper overview of the SCs in the field of electrical and optical and enhance their power conversion efficiency. It is operated by Poisson's equations along with continuity equations to model charge carrier behavior, including the p–n junction's electrostatic properties. The following form of Poisson's equation is applied [26]:

$$\frac{\partial}{\partial v}(\epsilon_o \epsilon_r \frac{\partial \psi}{\partial v}) = -q(h - e + C_D - C_A + \frac{N_{def}}{q}) \quad (1)$$

In this context, the electrostatic potential ψ, along with the acceptor concentration C_A, donor concentration C_D, and the concentration of traps N_{def}, are interconnected. The continuity equations, presented in Eqs. (2) and (3), illustrate the relationship between the carrier recombination rate and the current densities of holes J_h and electrons J_e in the semiconductor [26]:

$$\frac{\partial J_h}{\partial v} - R_h + G = \frac{\partial h}{\partial t} \quad (2)$$

$$\frac{\partial J_e}{\partial v} - R_e + G = \frac{\partial e}{\partial t} \quad (3)$$

In the specified equations, G denotes the carrier generation rate, R_e represents recombination rate of electron, and R_h indicates the recombination rate of holes. The drift current, represented by the symbols D_h (for electrons) and D_e (for holes), is given by Eqs. (4) and (5), respectively [27,28]:

$$J_e = qe\mu_e E - qD_e \frac{\partial e}{\partial v} \quad (4)$$

$$J_h = qe\mu_h E - qD_h \frac{\partial h}{\partial u} \quad (5)$$

This investigation focuses the design and simulation of a Cs_2TlRhI_6-based PSC utilizing SCAPS-1D to assess its optoelectronic properties. The SC design, shown in Fig. 1(a), includes a glass substrate, a transparent and conductive FTO layer, an ETL, the Cs_2TlRhI_6 layer, an HTL, and a back contact. To determine the optimal HTL, various candidates, including Cu_2O, CFTS, CuI, CuSCN, P3HT, Spiro, MoO_3, and, CdTe were analyzed while keeping TiO_2 fixed as the ETL. After evaluation, CdTe showed the best performance among them. CdTe as HTL has certain environmental and health concerns. So, Cu_2O is selected as HTL because it is a convenient and promising material for HTL performance [29]. Similarly, different ETLs such as SnS_2, TiO_2, IGZO, $Cd_{0.5}Zn_{0.5}S$, PCBM, ZnOS, and CdS were studied while maintaining Cu_2O as the fixed HTL, with IGZO demonstrating the best performance. Nickel served as the metal contact for the back owing to its advantageous electrical characteristics.

The material parameters considered in our work are outlined in Tables 1 and 2, respectively. The properties were sourced from previously published, peer-reviewed literature, thereby ensuring the accuracy and reliability of the simulation outcomes [28]. Furthermore, a uniform interface state density of 10^{10} cm^{-3} was considered across the whole simulation domain [26]. The simulations were performed with AM 1.5G illumination with an incidence power of 1000 W/m^2 and a reference temperature of 300 K. Resistances (series (Rs) and shunt (Rsh)) were initially configured to 1 $\Omega\,cm^{-2}$ and 1×10^6 Ω cm^{-2} respectively, prior to the optimization process. The simulation yielded the following PV performance metrics: the PCE of 16.41%, the J_{SC} of 39.94 mA/cm^2, the FF of 70.04%, and the V_{OC} of 0.59 V. The recorded values represent the initial state prior to the exploration of optimization and subsequent enhancements, which involved tuning of the physical parameters, interface defect densities, and external conditions.

3. Results & Discussion

3.1. DFT analysis

3.1.1. Structural properties of Cs_2TlRhI_6 compound

Cs_2TlRhI_6 adopts a double perovskite structure following the $A_2BB'X_6$ formulation, where Cs^+occupies the A-site, while Tl and Rh reside on the B-sites, and I^-acts as the halide. The compound is anticipated to the form of crystal in the high-symmetry cubic state most likely $Fm\bar{3}m$ (No. 225) space group characterized by minimal octahedral tilting. In this structure, Cs^+ ions coordinate with 12 I^-ions to form CsI_{12} cuboctahedra, which share corners with both TlI_6 and RhI_6 octahedra. Each of the TlI_6 and RhI_6 octahedra is built from six I^-ions, and these octahedral units interconnect with the CsI_{12} frameworks to generate a robust three-dimensional work. The detailed atomic arrangement is supported by the assigned Wyckoff positions: 4a Wyckoff site, at coordinates (0, 0, 0), is occupied by Rh; Tl is placed at 4b site having coordinates $(0.5, 0.5, 0.5)$; Cs is placed at 8c site having coordinates $(0.25, 0.25, 0.25)$; and I is lied at 24e site having coordinates

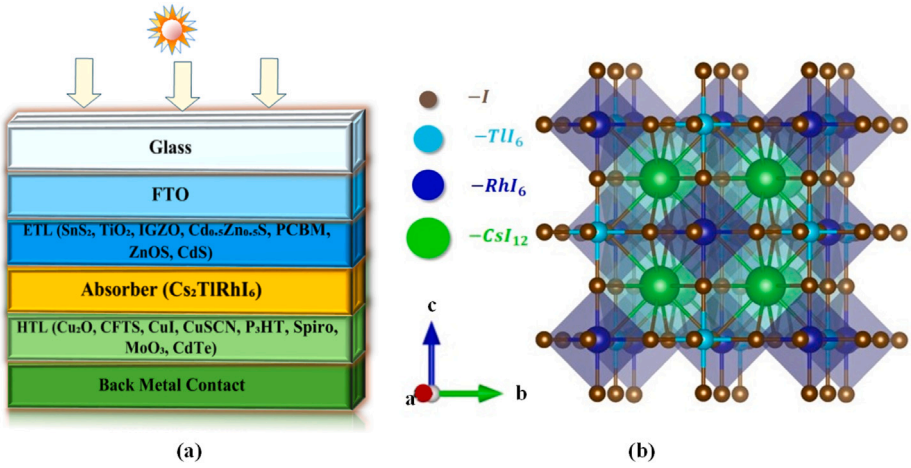

Fig. 1. (a) Depiction of the designed SC configuration and (b) crystallographic unit cell of the HDP.

$(0.2507, 0, 0)$. The structural stability of Cs_2TlRhI_6 can be assessed using Goldsmith's stability criteria. According to Goldsmith, octahedral factor (μ) along with tolerance factor (T_F) are defined as follows [10]:

$$T_F = R_X + R_Z/\sqrt{2}\left(\frac{R_{B'} + R_{B''}}{2} + R_Z\right) \tag{6}$$

$$\mu = R_{B'} + R_{B''}/2R_Z \tag{7}$$

here, R denotes the Shannon ionic radii corresponding to each element, where $X = Cs^+$ with a coordination number of 12, $B' = Tl^+$, $B'' = Rh^{3+}$, and $Z = I$ with a coordination number of 6. The calculated values of T_F and μ are 0.88 and 0.49, in that order. Both parameters lie within the ranges $0.80 < T_F < 1.1$ [30] and $0.414 < \mu < 0.89$ [31], thereby validating the structural stability. The optimized lattice constant is $a = 11.78$ Å, showing close agreement with the earlier reported value of 11.72 Å [10] obtained through GGA-PBE-based volume optimization. Furthermore, the formation energy plays a key role, where a negative value signifies the thermodynamic stability and structural robustness of the material. For the investigated compound, the computed formation energy is −3.016 eV per atom, expressed in the following equation [32]:

$$\Delta E = \left(\left[E\left(Cs_2TlRhI_6\right) - 2E(Cs) - E(Tl) - E(Rh) - 6E(I)\right]\right)/N \tag{8}$$

here, E(Cs), E(Tl), E(Rh), and E(I) represent energies of given materials Cs, Tl, Rh along with I in bulk form and $E\left(Cs_2TlRhI_6\right)$ represents the systems total energy and N represents how many atoms are in the system. The estimated formation energy of this double perovskite indicates strong structural stability.

3.1.2. Band dispersion and DOS study of Cs_2TlRhI_6

The electronic behavior of Cs_2TlRhI_6 can be explored effectively by evaluating its band profile and density of states (DOS). Important insights into the compound's band gaps, carrier states, and energy distributions are obtained through electronic structure analysis [26]. Fig. 2(a) presents the band dispersion of Cs_2TlRhI_6 along the Brillouin zone path W–L–Γ–X–W–K, calculated using the hybrid HSE06 functional. The Fermi level (E_F) is indicated by a red dotted line, set at the reference energy of 0 eV. Bands along with energy values below E_F are often termed as valence bands, and those with energy values more than E_F are referred to as conduction bands. From the observation, it was found that bands (valence along with conduction) do not cross over the Fermi level and also do not interfere with each other. The coincidence of the valence band top and conduction band bottom at the L point confirms that this compound displays a direct band gap of 1.12 eV. It is noted that Amin et al. calculated band gap values of 1.29 eV for Cs_2TlRhI_6 executing the exchange–correlation functional of TB-mBJ method, which is close to this result [29].

In Fig. 2(b), the partial along with the total DOS is utilized to highlight the contributions of specific atomic species and orbitals, shedding light on the chemical bonding characteristics of Cs_2TlRhI_6. As displayed in Fig. 2(b), the Fermi level (E_F) is marked by a vertical line at $E = 0$ eV. The energy states below E_F represent the occupied valence band states, while those above it correspond to the unoccupied conduction band states, extending up to approximately 1.1 eV. The computed band gap of 1.12 eV is consistent with the observed separation, confirming the semiconducting nature of the material. Below the Fermi energy, the TDOS is predominantly contributed by iodine 5p orbitals, along with notable involvement of rhodium 4d states. This indicates that the Rh atoms are essential to the bonding and electrical properties of the compound. The density of states decreases greatly above E_F, indicative of a band offset confirming the semiconducting nature of the compound. When viewed in the contextual nature of a projected DOS, the contributions of cesium 4d and thallium 6p can be seen as residual, indicating a less compelling role concerning the electronic structure. The iodine 5p and rhodium 4d orbitals are, therefore, especially relevant for light absorption and conductivity generation in the suggested device for solar applications.

3.1.3. Optical characteristics of Cs_2 $TlRhI_6$ material

Optical behavior are crucial for analyzing a material's response, as they arise from the interaction between electromagnetic energy, such as light, and the material's electrons. Sensoring these properties may give hints to applications, which might include their use in PSCs. To explore the optical characteristics of Cs_2TlRhI_6, we examine key parameters across a photon energy range from 0 to 10 eV. The complex dielectric function can be expressed as [10]:

$$\mathcal{E}(\omega) = \mathcal{E}\mathrm{r}(\omega) + i\mathcal{E}\mathrm{i}(\omega) \tag{9}$$

The energy-dependent components, $\mathcal{E}_i(\omega)$ and $\mathcal{E}_r(\omega)$, of the dielectric function $\mathcal{E}(\omega)$ are described using the Kramers–Kronig equation [10]:

$$\mathcal{E}_i(\omega) = \frac{e^2\hbar}{\pi m^2\omega^2}\sum_{v,c}\int_{BZ}\left|M_B(k)\right|^2\delta[\omega_B(k) - \omega]\,d^3k \tag{10}$$

$$\mathcal{E}_r(\omega) = 1 + \frac{2P}{\pi}\int_0^{\infty}\frac{\omega'\mathcal{E}_i(\omega')}{\omega'^2 - \omega^2}\,d\omega' \tag{11}$$

where P represents principal integral value, e is the charge of the electron, and $\hbar$ is the reduced Planck constant. The electron mass is represented by m, and ω indicates the angular frequency of the incoming photon. The term $M_B(k)$ corresponds to the dipole matrix element between conduction and valence band states. The Dirac delta function is represented by δ, $\omega_B(k)$ indicates the transition energy, and BZ signifies integration over the Brillouin zone.

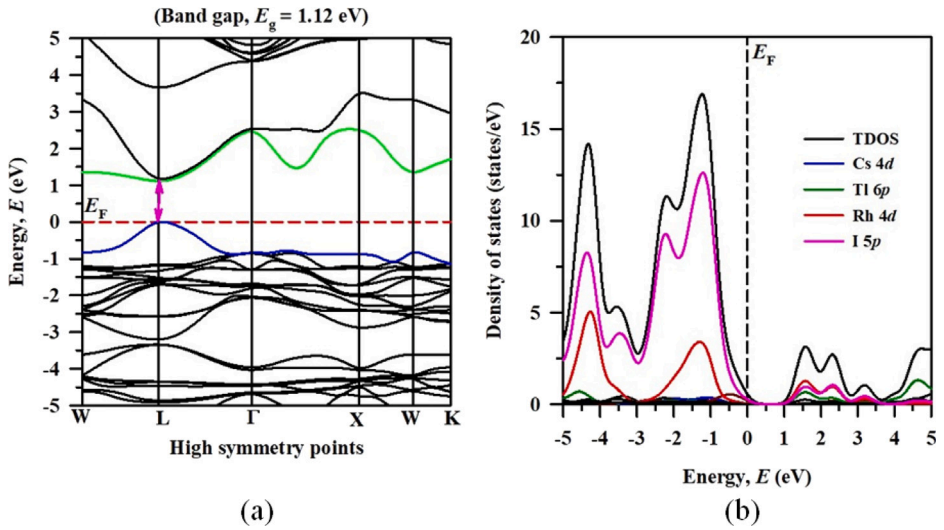

Fig. 2. (a) Estimated band structure and (b) DOS of Cs_2TlRhI_6. (For interpretation of the references to color in this figure legend, the reader is referred to the web version of this article.)

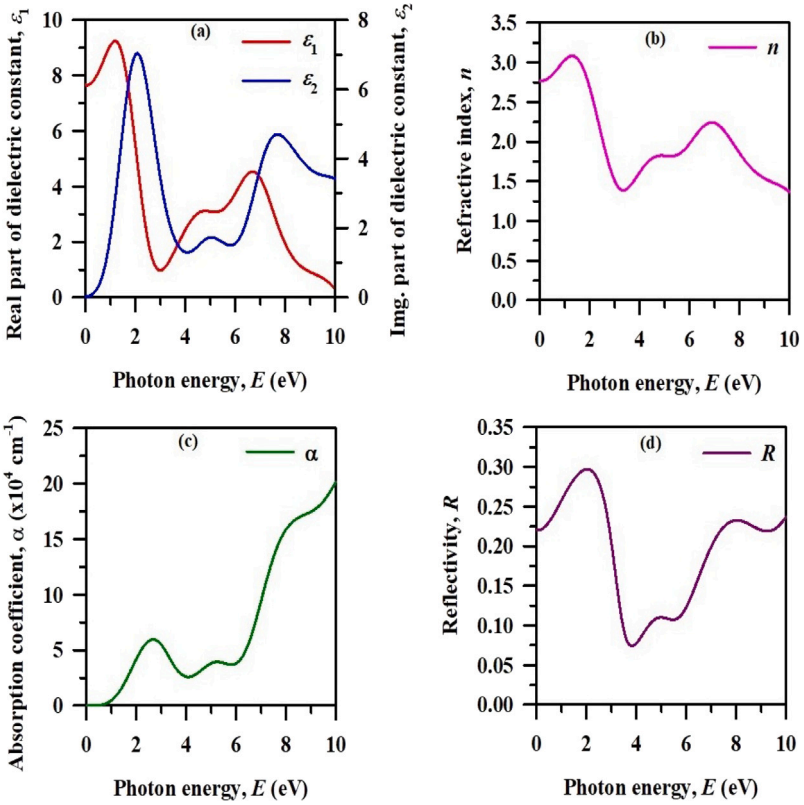

Fig. 3. (a) The real part of dielectric function's, $\varepsilon_1(\omega)$, and imaginary part, $\varepsilon_2(\omega)$, (b) material's refractive index $\eta(\omega)$, (c) material's coefficient of absorption $\alpha(\omega)$, and (d) material's reflectivity $R(\omega)$ of Cs_2TlRhI_6. (For interpretation of the references to color in this figure legend, the reader is referred to the web version of this article.)

The red curve in Fig. 3(a) represents the real component of the dielectric function, $\mathcal{E}_r(\omega)$. This component indicates the compound's ability to store electric energy. Here, $\mathcal{E}_r(\omega)$ starts at a high value for low photon energy and decreases as the photon energy increases. The peak value, which occurs around 1.15 eV, is approximately 9.2 and signifies strong electronic polarizability. At higher photon energies, the $\mathcal{E}_r(\omega)$ decrease occurs, meaning the material becomes less polarizable at these energies. The $\mathcal{E}_i(\omega)$, shown by the blue curve, displays sharp peaks that indicate strong optical absorption at specific photon energies. These features are linked to electronic transitions. The first noticeable peak appears near $E = 2$ eV, marking an important absorption feature close to the material's main absorption edge [10].

The real part of the refractive index in Fig. 3(b) is about 2.75 at zero photon energy. As photon energy increases, the refractive index also rises and reaches a maximum of roughly 3.1 at around 1.5 eV. This increase at lower energies shows that the material has a high optical density and interacts strongly with light. This trend agrees with the behavior of the dielectric function and supports the suitability of

Table 1
Physical parameters of selected HTLs and absorber.

Property[a]	CdTe	Spiro	P3HT	MoO_3	CuSCN	CuI	Cu_2O	CFTS	Cs_2TlRhI_6
t [nm]	200	150	150	100	150	150	150	150	500
E_g [eV]	1.5	2.88	1.7	3.0	3.4	2.98	2.17	1.3	1.12
χ [eV]	3.9	2.05	3.5	2.3	1.9	2.1	3.2	3.3	4.21
ε_r	9.4	3.0	3.0	18	10	6.5	7.1	3.5	7.6
N_C ($\times 10^{18}$ cm^{-3})	0.8	250	2000	10	17	28	250	2.2	42
N_V ($\times 10^{19}$ cm^{-3})	1.8	25	200	0.22	250	1.1	250	1.8	3
μ_e (cm^2 V^{-1} s^{-1})	320	0.0021	0.0018	210	0.0001	100	200	21.98	12.50
μ_h (cm^2 V^{-1} s^{-1})	40	0.0026	0.0186	210	1.0	43.9	8600	21.98	15.73
N_d (cm^{-3})	0	0	0	0	0	0	0	0	0
N_A ($\times 10^{18}$ cm^{-3})	0.0002	1.0	1.0	1.0	1.0	20	1.0	1.0	1
N_T ($\times 10^{15}$ cm^{-3})	1.0	1.0	0.1	1.0	0.1	1.0	1.0	1.0	1.0
References	[3]	[34]	[6]	[5]	[4]	[34]	[35]	[36]	This work

[a] t: thickness, χ: electron affinity, E_g: energy bandgap, ε_r: relative dielectric constant, N_C, N_V: effective density of states in conduction and valence bands, μ_e, μ_h: electron and hole mobilities, N_D, N_A: donor and acceptor concentrations, N_T: trap density.

the compound for photovoltaic and optoelectronic applications. The complex refractive index, $\tilde{n}(\omega)$ can be expressed as [10]:

$$\tilde{n}(\omega) = \left[\mathcal{E}_r(\omega) + i\mathcal{E}_i(\omega)\right]^{\frac{1}{2}} \tag{12}$$

The absorption parameter $\alpha(\omega)$ is determined according to the expression given below [10]:

$$\alpha(\omega) = \frac{\sqrt{2}\,\omega}{c}\left[\sqrt{\mathcal{E}_r^2(\omega) + \mathcal{E}_i^2(\omega)} - \mathcal{E}_r(\omega)\right]^{1/2} \tag{13}$$

The absorption coefficient is an important factor in evaluating materials for solar-cell applications because it shows how strongly the material absorbs light. As shown in Fig. 3(c), absorption is very low between 0 and 1.0 eV, but it begins to rise quickly once the photon energy reaches around 1.0 eV. This behavior matches the calculated band gap of 1.12 eV obtained using the hybrid functional. A strong absorption peak appears in the visible region, reaching about $6 \times 10^4\,cm^{-1}$ at roughly 2.75 eV, which suggests that the material can effectively absorb visible light for photovoltaic use. The reflectivity, which describes how much light is reflected from the surface, can be calculated from the real and imaginary parts of the dielectric function as described in Ref. [18].

$$R(\omega) = \left|\frac{1 - \sqrt{\mathcal{E}(\omega)}}{1 + \sqrt{\mathcal{E}(\omega)}}\right|^2 \tag{14}$$

The reflectivity, shown in Fig. 3(d), describes how much of the incoming light is reflected from the surface of the material. At 0 eV photon energy, the reflectivity is about 22%. As the photon energy increases, $R(\omega)$ rises and reaches a peak of around 29% near 2 eV, mainly due to interband electronic transitions. After this point, the reflectivity slowly decreases. Across the visible range (1.75–3.3 eV), the reflectivity stays below 30%, which suggests that the material absorbs light efficiently and supports its suitability for optoelectronic devices and solar cells [33].

3.2. SCAPS-1D results analysis

3.2.1. Selection of the optimal HTL for enhanced PV performance

Selecting an HTL is essential for creating extremely effective SCs. This work investigates eight distinct HTL materials: Cu_2O, CFTS, CuI, CuSCN, P3HT, Spiro, MoO_3 and CdTe to determine the material that delivers the best PV performance. Table 1 summarizes various HTL parameters sourced from peer-reviewed journals [28]. The material for ETL remains fixed as TiO_2 throughout this analysis (see Table 3).

Fig. 4(a) displays a comparative bar chart illustrating the output of various HTLs. Among the evaluated HTLs, CdTe exhibited the highest PCE, achieving a value of 25.125%. However, despite its high efficiency, the use of CdTe is associated with environmental and health concerns, which limits its viability for sustainable applications. From the above analysis, Cu_2O is selected as the most suitable HTL. Moreover, it is notable for its chemical stability and ease of fabrication, make it a strong contender for application in organic and PSCs [28]. The equation below is used to calculate the VBOs for different HTL materials [36]:

$$VBO = \left(\chi_{HTL} + E_{gHTL}\right) - \left(\chi_{abs} + E_{\text{gabs}}\right) \tag{15}$$

In this expression, χ_{abs} and χ_{HTL} represent the electron affinities of the Cs_2TlRhI_6 absorber and the HTL, respectively. The terms E_{gabs} and E_{gHTL} denote the energy bandgaps of the absorber layer and the HTL. Based on this formula and the values provided in Tables 1 and 2, the VBO values for Cu_2O, CuI, CuSCN, P3HT, Spiro, MoO_3, and CdTe are: 0.04 eV, −0.25 eV, −0.03 eV, −0.13 eV, −0.4 eV, −0.03 eV, and 0.07 eV, respectively. A positive value of VBO at the spaces between the HTL and perovskite layer forms a slight energy drop, often referred to as a cliff in the energy band structure [39]. This configuration facilitates effective hole transfer from the absorber to the HTL. Fig. 4(b) displays the energy band diagram of various HTLs, demonstrating their alignment with two bands (valence and conduction) of the absorber material. This band structure shows the energy of the valence band of Cu_2O being marginally less than the absorber valence band energy, which forms a cliff of 0.04 eV. It helps the Cu_2O to collect holes only and prevent electrons. Thus, it maintains good carrier selectivity. So, this analysis supports the choice of Cu_2O as an HTL. Using Cu_2O together with TiO_2 yields the following performance parameters: $V_{OC} = 0.587$ V; FF = 70.41%; $J_{SC} = 39.94$ mA/cm^2; PCE = 16.38%. Table 3 presents the VBO values along with the photovoltaic performance metrics of PSCs incorporating various HTLs paired with TiO_2.

3.2.2. Selection of the optimal ETL for enhanced photovoltaic performance

Different ETLs $\left(SnS_2, TiO_2, IGZO, Cd_{0.5}Zn_{0.5}S, PCBM, ZnOS, CdS\right)$ are analyzed to determine the finest execution. Here, Cu_2O remains fixed as the HTL. In contact with the absorber layer, the ETL is essential for collecting electrons and preventing recombination losses. Fig. 5(a) presents a comparative analysis of various ETLs in terms of PCE, FF, V_{OC}, and J_{SC}. Among them, IGZO demonstrated the best performance with the respective parameters: $V_{OC} = 0.587$ V, $J_{SC} = 39.94$ mA/cm^2, FF = 70.04%, and PCE = 16.41%. The following equation is used to determine conduction band (CBO) offset for the ETLs [36]:

$$CBO = \chi_{ABS} - \chi_{ETL} \tag{16}$$

here, χ_{ABS} refers to the electron affinity of Cs_2RhTlI_6, while χ_{ETL} corresponds to that of the ETL material. Based on this equation and the values provided in Table 2, the CBOs for SnS_2, TiO_2, IGZO, $Cd_{0.5}Zn_{0.5}S$, PCBM, ZnOS, and CdS are computed as: –0.05 eV, 0.31 eV, 0.05 eV, 0.41 eV, 0.31 eV, 0.71 eV, and 0.03 eV. IGZO has a tiny positive CBO of 0.05 eV. This forms a small spike at the conduction band edge. This

Table 2
Material properties of various ETLs and FTO.

Property[a]	ZnOS	CdS	$Cd_{0.5}Zn_{0.5}S$	SnS_2	TiO_2	PCBM	IGZO	FTO
t [nm]	30	30	30	30	30	50	30	200
E_g [eV]	2.83	2.4	2.8	1.85	3.2	2.0	3.05	3.5
χ [eV]	3.5	4.18	3.8	4.26	3.9	3.9	4.16	4.0
ϵ_r	9.0	10	10	17.7	9.0	3.9	10	9.0
N_C ($\times 10^{18}$ cm^{-3})	2.2	2.2	1.0	7.32	10.0	2500	5.0	2.2
N_V ($\times 10^{19}$ cm^{-3})	1.8	1.9	0.1	1.0	1.0	250	0.5	1.8
μ_e (cm^2 V^{-1} s^{-1})	100	100	100	50	20	0.2	15	20
μ_h (cm^2 V^{-1} s^{-1})	25	43.9	25	25	10	0.2	0.1	10
N_D ($\times 10^{18}$ cm^{-3})	1.0	0.1	0.1	0.985	0.1	2930	0.1	1.0
N_A (cm^{-3})	0	0	0	0	0	0	0	0
N_T ($\times 10^{15}$ cm^{-3})	1.0	1.0	1.0	0.1	0.1	1.0	0.1	1.0
References	[37]	[34]	[37]	[26]	[26]	[38]	[38]	[11]

[a] t: thickness, χ: electron affinity, E_g: energy bandgap, ϵ_r: relative dielectric constant, N_C, N_V: effective density of states in conduction and valence bands, μ_e, μ_h: electron and hole mobilities, N_D, N_A: donor and acceptor concentrations, N_T: trap density.

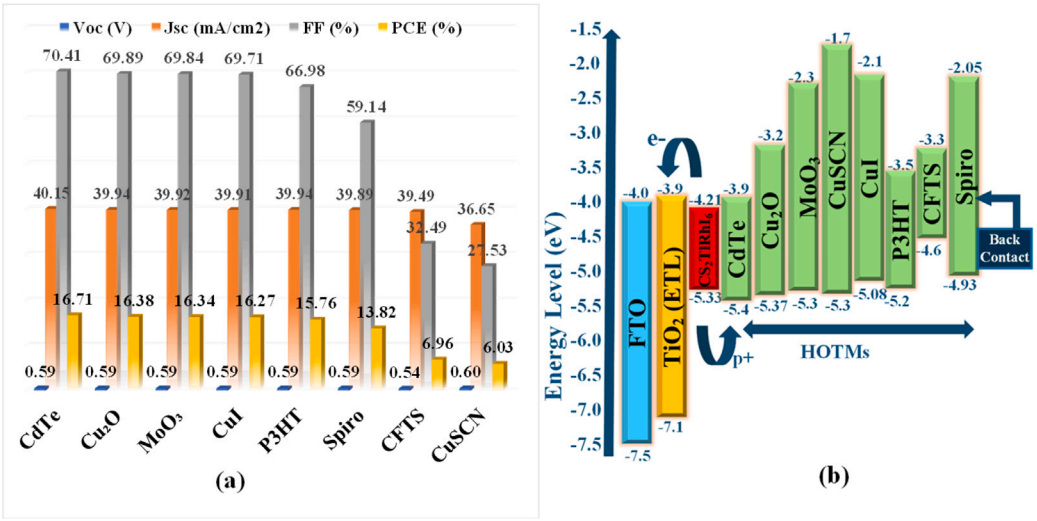

Fig. 4. Comparison of HTLs: (a) performance bar chart, (b) energy band diagram.

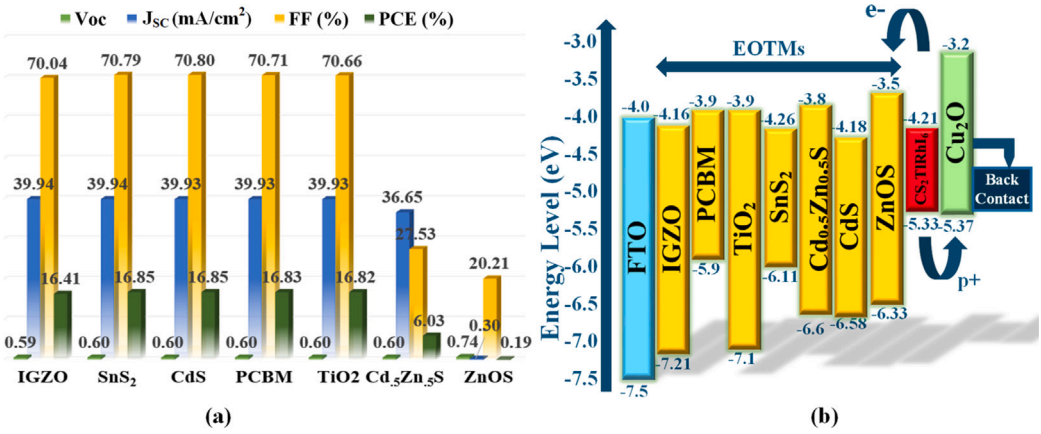

Fig. 5. Comparison of ETLs: (a) performance bar chart, (b) energy band diagram.

small spike helps to prevent electrons from returning to the perovskite from the ETL while maintaining effective energy level alignment of various ETLs with the absorber layer of Cs_2TlRhI_6. Further, its exceptional electron mobility and outstanding carrier transport characteristics [40] make it the most efficient ETL candidate for PSC. Table 4 presents the CBO values and the photovoltaic performance of PSCs incorporating various ETLs paired with Cu_2O.

3.2.3. *Selection of* Cu_2O *HTL thickness based on performance and fabrication feasibility*

The device metrics of PCE, J_{SC}, V_{OC}, and FF are evaluated for various Cu_2O thicknesses, are shown in Fig. 6(a). The graph shows that PCE, J_{SC}, and FF decrease as thickness increases, whereas FF shows a slight increase. Thicker layers lead to higher resistive losses and more charge recombination, so it is important to find a balance to maximize efficiency without adding too much loss [39]. Considering

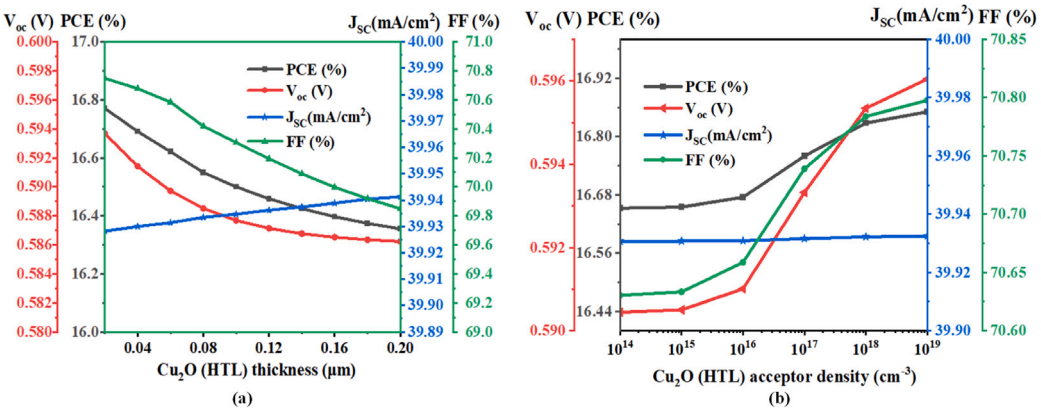

Fig. 6. Impact of HTL properties on PSC performance: (a) thickness and (b) acceptor density.

Table 3
Photovoltaic performance of PSCs incorporating various HTLs paired with TiO_2.

HTLs	VBO (eV)	PCE (%)	V_{OC} (V)	J_{SC} (mA/cm^2)	FF (%)
CdTe	0.07	16.71	0.591	40.15	70.41
Cu_2O	0.04	16.38	0.587	39.94	69.89
MoO_3	−0.03	16.34	0.586	39.92	69.84
CuSCN	−0.03	6.03	0.597	36.65	27.53
CuI	−0.25	16.27	0.585	39.91	69.71
P3HT	−0.13	15.76	0.589	39.94	66.98
Spiro	−0.40	13.82	0.586	39.89	59.14
CFTS	−0.73	6.96	0.543	39.49	32.49

Table 4
Comparison of PSC performance for different ETLs paired with Cu_2O.

ETLs	CBO (eV)	PCE (%)	V_{OC} (V)	J_{SC} (mA/cm^2)	FF (%)
IGZO	0.05	16.41	0.587	39.94	70.04
SnS_2	−0.05	16.85	0.596	39.94	70.79
CdS	0.03	16.85	0.596	39.93	70.80
PCBM	0.31	16.83	0.596	39.93	70.71
TiO_2	0.31	16.82	0.596	39.93	70.66
$Cd_{0.5}Zn_{0.5}S$	0.41	6.03	0.597	36.65	27.53
ZnOS	0.71	0.19	0.741	0.30	83.49

fabrication feasibility, prior studies by Chatterjee et al. demonstrated that Cu_2O thin films in the 40–50 nm range provide efficient carrier mobility and minimized losses of recombination [41]. The SILAR and solution-processed methods used in those studies ensured controlled and uniform Cu_2O deposition, which is critical for high device performance [41,42]. In this study, a 50 nm Cu_2O HTL thickness is selected, as it achieves a J_{SC} of 39.93 mA/cm^2, PCE of 16.65%, V_{OC} of 0.59 V, and a FF of 70.63%. This selection aligns with the reported optimal range, ensuring both high performance and practical manufacturability. Therefore, 50 nm is chosen as the optimal thickness, balancing efficiency gains and fabrication feasibility.

3.2.4. *Effect of the acceptor density of* Cu_2O *(HTL)*

Fig. 6(b) shows how the performance changes with varying HTL acceptor density. As the acceptor concentration increases, the PCE improves, reaching about 24.88% at $N_A = 10^{17}$ cm^{-3}. The V_{OC} also increases steadily and becomes roughly 0.81 V at this level. The J_{SC} stays almost unchanged but shows a small rise at higher acceptor densities, helping boost the efficiency. The FF follows a similar upward trend before becoming stable. Overall, these results show that choosing an appropriate acceptor density in the Cu_2O helps improve charge transport and reduces recombination, which leads to better device performance [2].

To support these findings experimentally, Jo et al. grew Cu_2O thin films using RF magnetron sputtering and then annealed the films at 600 °C in a vacuum. This process produced hole carrier concentrations between 10^{15} and 10^{17} cm^{-3} [43]. The film thickness measured by ellipsometry ranged from 10 to 80 nm. The acceptor density of $N_A = 10^{17}$ cm^{-3} aligns well with these fabrication results and corresponds to the highest observed PCE and V_{OC}, confirming that this value represents an optimal condition for improving PSC performance.

3.2.5. *Effect of absorber thickness*

Fig. 7(a) presents how the absorber layer thickness affects the main photovoltaic parameters of the PSC. As the thickness increases, both PCE and J_{SC} rise sharply at lower values and then begin to saturate beyond about 0.6 μm. This trend suggests that a thicker absorber enhances light absorption and charge generation until the point where additional thickness no longer contributes significantly. In contrast, V_{OC} and the FF slowly decrease as the absorber layer becomes thicker. This drop is mainly due to stronger recombination and higher internal resistance in the bulk of the material [16,35].

An absorber thickness of 0.8 μm was found to be the best choice because it offers a good balance between PCE and V_{OC}. At this thickness, the PCE reaches 16.86%, J_{SC} is 41.82 mA/cm^2, V_{OC} is 0.58 V, and the FF is 70.44%. Increasing the thickness further brings only a small gain in photocurrent but increases recombination. For this reason, keeping the absorber thickness close to 0.8 μm helps maintain good carrier collection, lower losses, and stable performance of the PSC.

3.2.6. *Impact of absorber acceptor density*

In this study, Cs_2TlRhI_6 was used as the absorber material, and its acceptor density (N_A) was examined to evaluate its effect on PSC efficiency. The N_A was varied from 1×10^{14} cm^{-3} to 1×10^{19} cm^{-3}. Fig. 7(b) shows a positive correlation between N_A and key PV metrics, with the highest values observed at 1×10^{19} cm^{-3}. At this optimal density, the PCE reaches 25.83%, the highest recorded in this study. The V_{OC} increases to 0.79 V, reflecting improved charge separation and reduced recombination. J_{SC} decreases to 40.53 mA/cm^2 as the acceptor density rises. The FF increases to 80.54%, showing improved charge transport due to reduced series resistance (R_S). These results indicate that increasing the absorber N_A enhances carrier concentration and charge transport, thereby improving photovoltaic performance.

3.2.7. *Selection of appropriate ETL thickness*

IGZO has been widely studied as an ETL owing to its high charge mobility and superior transport characteristics [40]. Cho et al. previously demonstrated that IGZO thin films produced through Atomic Layer Deposition (ALD) and RF magnetron sputtering and show significant variations in material quality [40]. IGZO films deposited via ALD demonstrated enhanced film density, reduced oxygen vacancies, and an increased mobility of 36.6 cm^2/V s, in contrast to sputtered films that displayed a mobility of 20.1 cm^2/V s [40]. Hsu et al. investigated

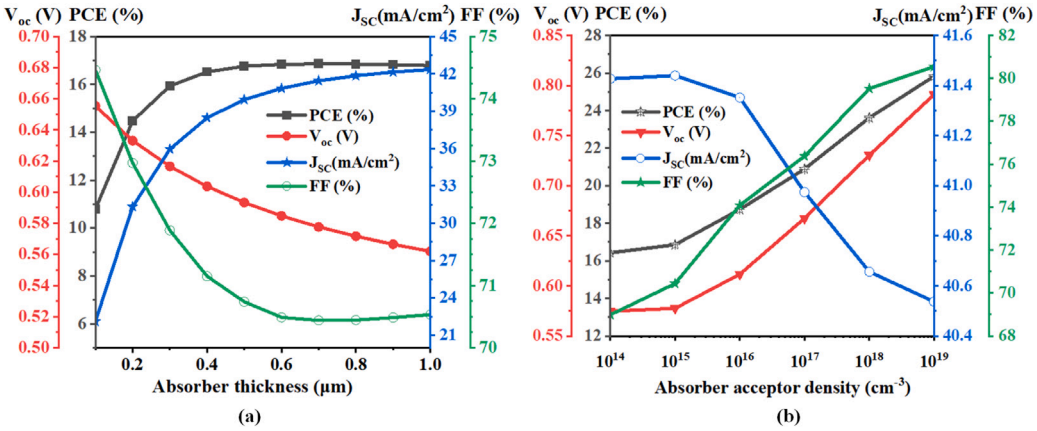

Fig. 7. Impact of Cs_2TlRhI_6 properties on SC PV metrics: (a) thickness and (b) acceptor density.

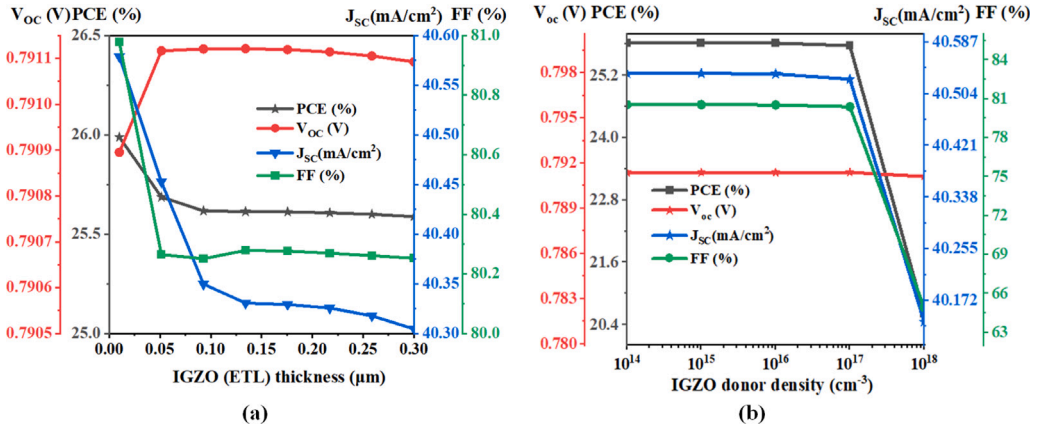

Fig. 8. Influence of ETL properties on PSC performance: (a) thickness, and (b) donor density.

flexible IGZO transistors on polycarbonate substrates, optimizing the thickness of IGZO between 25 and 45 nm, and reached 76 $cm^2/V\,s$ for the maximum field-effect mobility with a stacked $SiO_2/TiO_2/SiO_2$ (STS) dielectric [44]. The studies indicate that IGZO thickness between 16 and 45 nm is optimal for high-performance devices, with ALD yielding superior material quality, whereas sputtering is favored for flexible applications. The influence of IGZO thickness variation between 0.01 μm and 0.30 μm on SC output is presented in Fig. 8(a). The findings show that optimal efficiency within this range is yielded through an IGZO thickness of 0.03 μm. Increasing the ETL thickness above 0.03 μm results in a decrease in performance. The findings match with prior research [40,44], indicating that thin IGZO layers (approximately 30 nm) improve charge transport and device efficiency. The optimal performance at 0.03 μm demonstrates that an appropriately adjusted IGZO thickness enhances electron mobility and reduces recombination losses, thereby serving as a critical element in attaining high-performance PSCs.

3.2.8. Selection of appropriate ETL donor density

Fig. 8(b) illustrates the influence of IGZO donor density on the key photovoltaic parameters of PCE, V_{OC}, J_{SC}, and FF on the PSC. As shown in the figure, the PCE, J_{SC}, and FF remain relatively stable as the donor density increases from 10^{14} to 10^{17} cm^{-3}. In this range, carrier transport and charge extraction are efficient, and recombination losses are minimal. However, when the donor density increases beyond 10^{17} cm^{-3}, a sharp decline is observed in all performance metrics. This reduction is primarily due to enhanced recombination at the interface and increased carrier scattering, which deteriorate charge collection efficiency. Therefore, an optimum donor concentration of 10^{16} cm^{-3} is selected, ensuring high efficiency without introducing performance degradation. At this point, the parameters obtained are: V_{OC} = 0.79 V, J_{SC} = 40.53 mA/cm^2, FF = 80.40%, and PCE = 25.78%.

3.2.9. Selection of back metal contact

Choosing the right back metal contact (BMC) is essential to maximizing perovskite SCs' efficiency. The impact of changes in the work function of BMC materials on important photovoltaic parameters is examined in Fig. 9(a). The findings shows the improvement in PCE with a increasing in the BMC work function from 4.8 eV to 6 eV, stabilizing PCE at about 25.78% for work functions greater than 5 eV. It is noted that V_{OC} and J_{SC} remained relatively stable. The FF exhibited an upward trend, attaining approximately 80.40% at elevated work functions, therefore, Ni was identified as our BMC for its favorable work function of 5.5 eV, cost-effectiveness, availability, and efficiency [35]. Its incorporation as a BMC promotes effective charge extraction, suppresses carrier recombination, and contributes to improved overall device operation.

3.2.10. Impact of series resistance (R_S)

The impact of R_S on the photovoltaic parameters was investigated to better understand its effect. Increasing R_S leads to a decrease in V_{OC} due to power losses and recombination, thus reducing the overall PCE. As shown in Fig. 9(b), the performances of devices decrease with increasing R_S from 0 to 6 $\Omega\,cm^{-2}$. As R_S further increases, the PCE decreases from 27.28% to 18.50%, and the FF reduces from 85.12% to 57.89%. This almost linear decay corresponds to the trend found in other studies [27,45,46]. The charge collection efficiency decreases with increasing R_S since it introduces a resistive loss in the detector. To

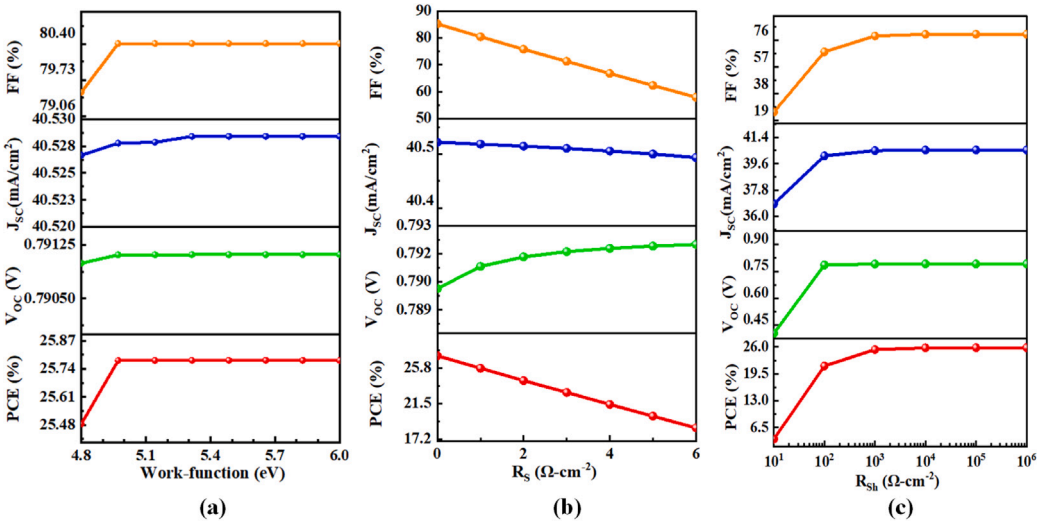

Fig. 9. Effect of different parameters on the performance of SC: (a) back contact work function, (b) series resistance, and (c) shunt resistance.

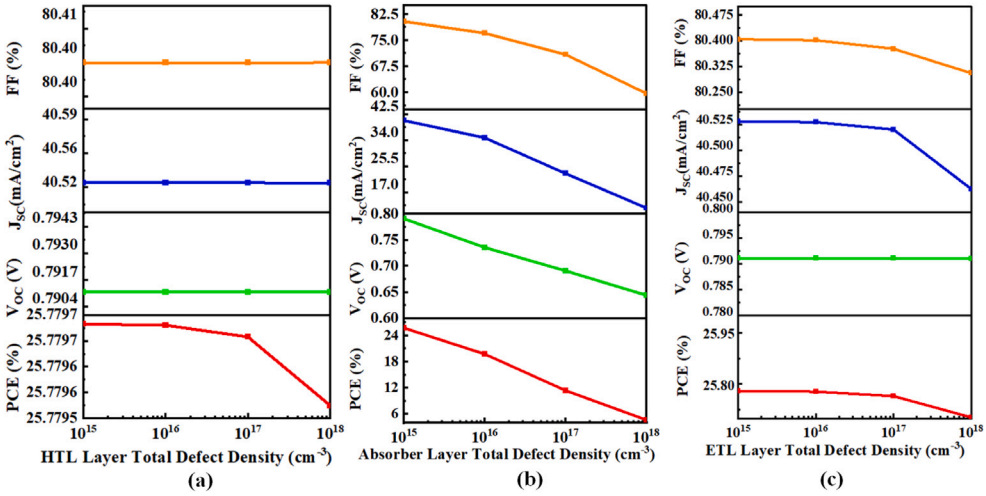

Fig. 10. Analysis of PSC performance variation with total trap density: (a) Cu_2O layer, (b) absorber (Cs_2TiRhI_6), and (c) IGZO layer.

be consistent with the experimental and simulation results, we take a typical $R_S = 1\,\Omega\,cm^{-2}$ as reported previously [27,45]. This value gives a more realistic and practical estimate for the PSCs, so that their intrinsic performances can be accurately modeled at the standard operating conditions. It can be concluded from this analysis that R_S dominates the performance of PSCs. Reducing R_S using better charge transport layers and optimal interfaces is important for further improving the performance.

3.2.11. Impact of shunt resistance (R_{sh})

A higher shunt resistance is beneficial as it reduces leakage currents and enhances charge extraction [39]. As shown in Fig. 9(c), the photovoltaic parameters change clearly with variations in R_{sh}. The best performance is obtained at $R_{sh} = 1 \times 10^5\,\Omega\,cm^{-2}$, where the device reaches a PCE of 25.78%, $J_{SC} = 40.53\,mA/cm^2$, $V_{OC} = 0.79\,V$, and an FF of 80.40%. These results agree well with earlier simulation work by Bimli et al. [28] and Sunny et al. [47], both of whom also used $R_{sh} = 1 \times 10^5\,\Omega\,cm^{-2}$ in their studies. When R_{sh} decreases, leakage current increases noticeably, which lowers both V_{OC} and FF and ultimately reduces the PCE [28]. These observations show that careful interfacial band alignment and good surface passivation are important for keeping R_{sh} high and ensuring stable, high-efficiency PSC operation.

3.2.12. Analysis of defect density on different layers

The effect of total defect density on the device performance was examined for the HTL, absorber, and ETL layers. Fig. 10 shows how the main PV parameters change as the defect density varies in each layer. For the HTL (Cu_2O), increasing the defect density from 10^{15} to 10^{18} cm^{-3} causes only small changes in J_{SC}, V_{OC}, and FF, so the PCE stays almost the same. This means that, within this range, defects in the HTL do not strongly affect the overall performance of the device.

The absorber layer (Cs_2TlRhI_6), however, shows a much stronger response. As the defect density increases from 10^{15} to 10^{18} cm^{-3}, the PCE drops sharply from 25.78% to about 5%. This decrease is also reflected in lower values of J_{SC}, V_{OC}, and FF. The primary cause of this decline is the increase in non-radiative recombination. This shortens the carrier lifetime and reduces charge extraction efficiency.

For the ETL (IGZO), the trend is similar but less severe. While V_{OC} changes very little, higher defect density leads to noticeable reductions in J_{SC} and FF, resulting in a lower PCE. Overall, these results show that defects in the absorber layer have the strongest impact on device performance, followed by moderate effects from the ETL and very small effects from the HTL. To keep the comparison consistent, a defect density of 10^{15} cm^{-3} was used as the baseline for all simulations.

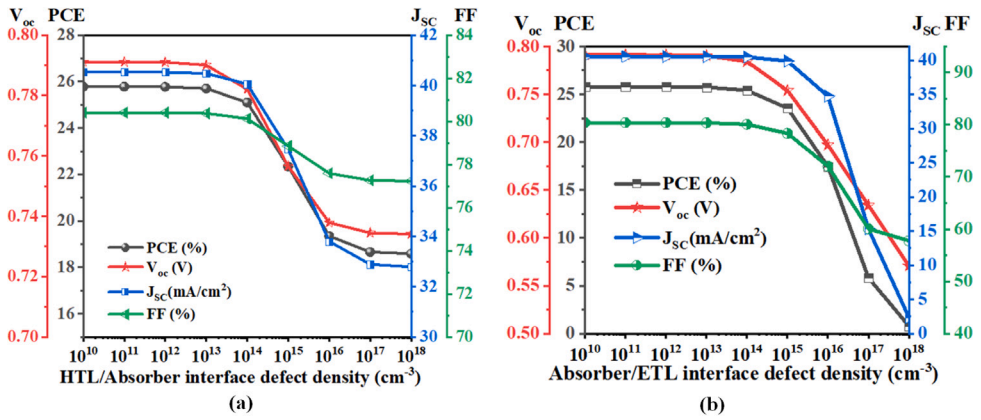

Fig. 11. Analysis of defect density at interfaces: (a) Cu_2O/Cs_2TiRhI_6, and (b) Cs_2TiRhI_6/IGZO.

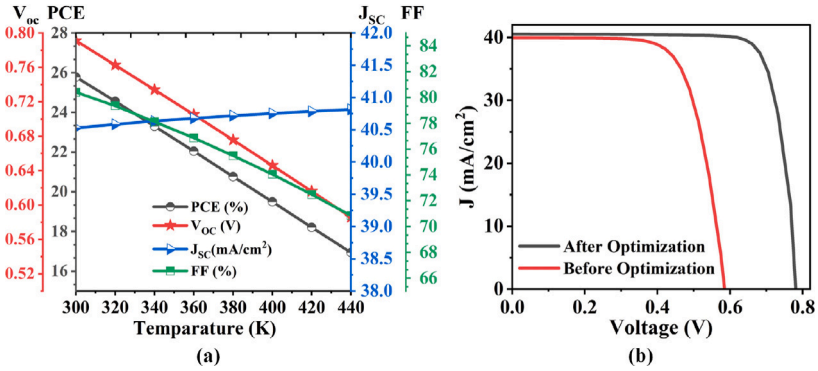

Fig. 12. (a) Temperature-dependent variations in the PV metrics, (b) J–V comparison before and after optimization. (For interpretation of the references to color in this figure legend, the reader is referred to the web version of this article.)

3.2.13. Analysis of interface defects on different layers

In SCAPS simulations, the default interface defect density for all layers is set to 1×10^{10} cm^{-3}. To examine how interfacial defects affect device performance, defect densities were systematically varied at both interfaces. Fig. 11(a) illustrates that an increase in defect density at the HTL/absorber boundary results in a gradual drop in PV metrics, as the defect level rises from 1×10^{10} cm^{-3} to 1×10^{18} cm^{-3}. A comparable trend is evident in Fig. 11(b), which focuses on the absorber/ETL interface. Performance degradation mainly results from a non-radiative recombination at elevated interface trap densities, which shortens carrier lifetimes and lowers charge extraction efficiency [48].

3.2.14. Temperature effects on performance parameters

The effect of temperature on the performance of the optimized Cs_2TlRhI_6-based device was studied in the range of 300–440 K. As the temperature increased, V_{OC}, J_{SC}, FF, and PCE all showed a gradual decrease. The V_{OC} dropped from 0.791 V at 300 K to 0.586 V at 440 K, mainly because of stronger non-radiative recombination and thermally activated defect states in the absorber layer [20]. The J_{SC} remains nearly constant. It indicates that carrier generation was only weakly affected by temperature [39]. In contrast, both FF and PCE showed a gradual reduction from 80.40% and 25.78% at 300 K to 74.05% and 19.49% at 400 K, respectively. This decline can be attributed to increased recombination losses and lower carrier mobility at higher temperatures [19]. Despite this reduction, the device retains more than 90% of its original performance up to 350 K, showing that Cs_2TlRhI_6 has excellent thermal stability.

3.2.15. Optimized results

Fig. 12(b) shows the J–V characteristics of the PSC before and after optimization. The optimized device, shown by the black curve, performs much better than the unoptimized one, represented by the red curve. The V_{OC} increased from 0.587 V to 0.791 V, which is about a 34.7% improvement and indicates lower recombination losses. The J_{SC} rose slightly from 39.9 mA/cm^2 to 40.53 mA/cm^2, showing better light absorption and charge transport. The FF improved from 70.0% to 80.40%, suggesting more efficient band alignment between the ETL and HTL. Overall, the optimization raised the PCE from 16.4% to 25.78%, giving an absolute improvement of about 9.4%.

4. Comparison with other work

Table 5 summarizes and compares the results of this study with previously reported PSCs-based works. In 2022, Zhang et al. experimentally produced hydrogenated $Cs_2AgBiBr_6$ films and achieved a PCE of 6.37%, showing longer carrier lifetime and better stability [49]. After that, in 2024, Xiang et al. demonstrated that introducing a $Cs_2AgBiBr_6$ interlayer improved both efficiency and stability. Their fabricated device reached a PCE of 19.52% with a V_{OC} of 1.12 V [50]. These experimental studies provided useful insights into the potential of double perovskites, though performance was still limited by low current density and interfacial losses.

In addition to these experimental efforts, several theoretical studies have focused on improving device performance and exploring new absorber materials. Recently, in 2025, Utsho et al. reported that using CBTS as the hole transport layer in a $Cs_2CuBiBr_6$ device increased efficiency to 19.70% [51], showing how the choice of transport materials affects device performance. Ferdous et al. [52] and Hossen

Table 5
Comparing photovoltaic parameters with existing research.

Device	V_{OC}	J_{SC}	FF	PCE	Ref.
ITO/SnO_2/$Cs_2AgBiBr_6$/spiro-OMeTAD/Au	0.92	11.4	60.93	6.37	[49]
FTO/WS_2/$Cs_2CuBiBr_6$/spiro-OMeTAD/Ag	0.60	34.59	67.36	14.08	[54]
ITO/WS_2/$Cs_2CuBiBr_6$/CBTS/Ni	0.712	35.63	77.57	19.70	[51]
FTO/SnO_2/$Cs_2TiI_2Br_4$/CuSCN/Au	–	–	–	23.41	[52]
FTO/ZnOS/$Cs_2AgBi_{1-x}Sb_xBr_6$/Cu_xO/Au	1.46	18.12	89.88	23.81	[53]
ITO/LBSO/Cs_2TiBr_6/CNTS/Au	1.123	26.63	82.94	24.82	[55]
FTO/IGZO/Cs_2TlRhI_6/Cu_2O/Ni	0.922	41.73	83.15	25.78	This work

et al. [53] predicted PCE values of 23.41% for $Cs_2TiI_2Br_4$ and 23.81% for $Cs_2AgBi_{1-x}Sb_xBr_6$, respectively, indicating ongoing progress in absorber and interface optimization. In comparison, our presented work reached a theoretical PCE of 25.78%, surpassing all previously reported double PSCs.

5. Toxicity considerations

The studied material (Cs_2TlRhI_6) shows promising optoelectronic properties for photovoltaic applications. However, its practical implementation is limited by concerns regarding thallium (Tl) toxicity. Similar to Pb-based perovskites, Tl-containing compounds pose significant health and environmental risks due to their high toxicity, water solubility, and potential for bioaccumulation. Dipta et al. demonstrated that effective encapsulation strategies can substantially improve perovskite stability and mitigate heavy-metal leakage, underscoring the importance of physical barrier layers in reducing environmental hazards [56].

Several approaches, including hydrophobic surface coatings, toxic-ion-absorbing interlayers based on ionogels or resins, and advanced encapsulation methodologies, have been developed to minimize metal ion release from perovskite solar cells [56,57]. For Cs_2TlRhI_6 specifically, reducing Tl^+ ion migration should be considered a critical requirement for practical deployment. Furthermore, the establishment of effective disposal and recycling systems will be essential to ensure safe handling throughout the material and device life cycle.

6. Conclusion

In this work, we studied the structural and photovoltaic properties of the cubic double perovskite Cs_2TlRhI_6. The formation enthalpy and the Goldschmidt tolerance factor confirm that the material is structurally stable. Our DFT results show that Cs_2TlRhI_6 has a direct bandgap of about 1.12 eV, which is suitable for solar-cell use. The material also has a strong light absorption coefficient of $6 \times 10^4\ cm^{-1}$ at 2.75 eV, along with low reflectivity (below 30%) and a refractive index higher than 3.1, both favorable optical features for photovoltaic applications. Among the device configurations studied, the structure FTO/IGZO/Cs_2TlRhI_6/Cu_2O/Ni produced the best performance. This setup reached an efficiency of 25.78% with a fill factor of 80.40%. The device also kept more than 90% of its efficiency up to 350 K, showing good thermal stability.

However, despite these promising results, the use of thallium remains a concern because of its environmental and health risks. Therefore, further studies on safe handling, encapsulation, and recycling processes are necessary to mitigate potential risks. In summary, our findings indicate that Cs_2TlRhI_6 is a stable and efficient lead-free double perovskite material, holding significant promise for next-generation photovoltaic applications.

Declaration of competing interest

The authors declare that they have no known competing financial interests or personal relationships that could have appeared to influence the work reported in this paper.

Acknowledgments

The authors wish to express their gratitude to the Department of EEE and the Office of R&E at Rajshahi University of Engineering & Technology (RUET), Bangladesh, for their support and financial assistance.

References

[1] C. Gong, C. Zhang, Q. Zhuang, H. Li, H. Yang, J. Chen, Z. Zang, Stabilizing buried interface via synergistic effect of fluorine and sulfonyl functional groups toward efficient and stable perovskite solar cells, Nano-Micro Lett. 15 (1) (2023) 17.
[2] M.M. Hasan, A. Khaleque, T. Alam, Highly efficient lead-free solar cell using perovskite and chalcogenide materials, Sol. Energy 302 (2025) 114055.
[3] K. Fatema, Optimizing inorganic double halide (Cs_2TiI_6) perovskite solar cell for different hole transport layers using solar cell capacitance software (SCAPS-1D), Mater. Today Commun. 35 (2023) 105860.
[4] F. Azri, A. Meftah, N. Sengouga, A. Meftah, Electron and hole transport layers optimization by numerical simulation of a perovskite solar cell, Sol. Energy 181 (2019) 372–378.
[5] M. Shamna, K. Sudheer, Device modeling of Cs_2PtI_6-based perovskite solar cell with diverse transport materials and contact metal electrodes: a comprehensive simulation study using solar cell capacitance simulator, J. Photonics Energy 12 (3) (2022) 032211–032211.
[6] Y. Raoui, H. Ez-Zahraouy, N. Tahiri, O. El Bounagui, S. Ahmad, S. Kazim, Performance analysis of $MAPbI_3$ based perovskite solar cells employing diverse charge selective contacts: Simulation study, Sol. Energy 193 (2019) 948–955.
[7] B. Saparov, J.-P. Sun, W. Meng, Z. Xiao, H.-S. Duan, O. Gunawan, D. Shin, I.G. Hill, Y. Yan, D.B. Mitzi, Thin-film deposition and characterization of a Sn-deficient perovskite derivative Cs_2SnI_6, Chem. Mater. 28 (7) (2016) 2315–2322.
[8] A.P. Yadav, A.K. Bhojani, K. Bhargava, D.K. Singh, Impact of structural strain on performance of halide perovskite solar cells: A combined DFT and SCAPS-1D analysis, Adv. Theory Simul. 7 (11) (2024) 2400407.
[9] M.M. Hasan, M. Siddika, M.F. Ali, M.R.I. Sheikh, A. Al Mamun, M.J. Hossen, et al., Next-generation lead-free solar cells with $MASnBr_3$/$ZnSnN_2$ dual absorbers for high efficiency, Front. Mater. 12 (2025) 1652733.
[10] M. Amin, A. ul Haq, G. Mustifa, A. Afaq, S.M. Ramay, R. Sharma, A. Hanif, et al., Cs_2TlRhX_6 (X=Cl, Br, I): promising halide double perovskites for efficient energy harvesting in photovoltaic and thermoelectric applications, Phys. Scr. 98 (12) (2023) 125983.
[11] M.K. Hossain, A. Arnab, R.C. Das, K. Hossain, M. Rubel, M.F. Rahman, H. Bencherif, M. Emetere, M.K. Mohammed, R. Pandey, Combined DFT, SCAPS-1D, and wxAMPS frameworks for design optimization of efficient Cs_2BiAgI_6-based perovskite solar cells with different charge transport layers, RSC Adv. 12 (54) (2022) 35002–35025.
[12] P. Rohit, G.-P. Aryeh, L. Tomas, C. Bert, B. Aslihan, B. Hans-Gerd, et al., Band gap tuning via lattice contraction and octahedral tilting in perovskite materials for photovoltaics, 2017.
[13] X. Yang, Y. Chen, P. Liu, H. Xiang, W. Wang, R. Ran, W. Zhou, Z. Shao, Simultaneous power conversion efficiency and stability enhancement of $Cs_2AgBiBr_6$ lead-free inorganic perovskite solar cell through adopting a multifunctional dye interlayer, Adv. Funct. Mater. 30 (23) (2020) 2001557.
[14] G.F. Toki, M.K. Hossain, M.S. Uddin, A.M. Tawfeek, S. Rabhi, M.A. Darwish, R. Haldhar, D. Dwivedi, J. Madan, R. Pandey, Unveiling the potential of lead-free $Cs_2AgBi_{0.75}Sb_{0.25}Br_6$ double perovskite solar cells with multilayer charge transport for 30% efficiency, Inorg. Chem. Commun. 165 (2024) 112439.
[15] G.I. Toki, M.K. Hossain, R. Pandey, S. Bhattarai, A.M. Tawfeek, S. Mohammad, A. Habib, N. Mahmud, M.F. Rahman, P. Sasikumar, et al., Optimizing lead-free $Cs_3Bi_2I_9$ perovskite solar cells: exploring absorber and charge transport layers parameters for improved efficiency, J. Opt. 53 (5) (2024) 4554–4570.
[16] M.K. Hossain, M.K. Mohammed, R. Pandey, A. Arnab, M. Rubel, K. Hossain, M.H. Ali, M.F. Rahman, H. Bencherif, J. Madan, et al., Numerical analysis in DFT and SCAPS-1D on the influence of different charge transport layers of $CsPbBr_3$ perovskite solar cells, Energy Fuels 37 (8) (2023) 6078–6098.

[17] H. Sabbah, Z. Abdel Baki, R. Mezher, J. Arayro, SCAPS-1D modeling of hydrogenated lead-free $Cs_2AgBiBr_6$ double perovskite solar cells with a remarkable efficiency of 26.3%, Nanomaterials 14 (1) (2023) 48.

[18] O.R. Lunge, B.K. Ravidas, S. Bhattarai, R. Pandey, J. Madan, M.K. Roy, M.K. Hossain, D.P. Samajdar, DFT and SCAPS-1D based optimization study of double perovskite $Cs_2AuBiCl_6$ solar cells utilizing different charge transport layers, J. Phys. Chem. Solids 195 (2024) 112260.

[19] Q. Meng, Y. Chen, Y.Y. Xiao, J. Sun, X. Zhang, C.B. Han, H. Gao, Y. Zhang, H. Yan, Effect of temperature on the performance of perovskite solar cells, J. Mater. Sci., Mater. Electron. 32 (2021) 12784–12792.

[20] P. Lopez-Varo, M. Amara, S. Cacovich, A. Julien, A. Yaïche, M. Jouhari, J. Rousset, P. Schulz, J.-F. Guillemoles, J.-B. Puel, Temperature effects on the energy yield of perovskite solar cells, in: 2021 IEEE 48th Photovoltaic Specialists Conference, PVSC, IEEE, 2021, pp. 1089–1091.

[21] A.H. Slavney, L. Leppert, A. Saldivar Valdes, D. Bartesaghi, T.J. Savenije, J.B. Neaton, H.I. Karunadasa, Small-band-gap halide double perovskites, Angew. Chem. 130 (39) (2018) 12947–12952.

[22] J.P. Perdew, K. Burke, M. Ernzerhof, Generalized gradient approximation made simple, Phys. Rev. Lett. 77 (18) (1996) 3865.

[23] M. Segall, P.J. Lindan, M.a. Probert, C.J. Pickard, P.J. Hasnip, S. Clark, M. Payne, First-principles simulation: ideas, illustrations and the CASTEP code, J. Phys.: Condens. Matter. 14 (11) (2002) 2717.

[24] M. Ali, M.A. Hossain, M. Rayhan, M. Hossain, M. Uddin, M. Roknuzzaman, K. Ostrikov, A. Islam, S. Naqib, First-principles study of elastic, electronic, optical and thermoelectric properties of newly synthesized $K_2Cu_2GeS_4$ chalcogenide, J. Alloys Compd. 781 (2019) 37–46.

[25] R. Schira, C. Latouche, DFT and hybrid-DFT calculations on the electronic properties of vanadate materials: theory meets experiments, New J. Chem. 44 (27) (2020) 11602–11607.

[26] N.K. Singh, A. Agarwal, A.K. Singh, S.N. Singh, Design and performance evaluation of eco-friendly $FASnI_3/CsSn_{0.5}Ge_{0.5}I_3$ based perovskite solar cell with distinct charge transport layer: A computational modeling, Sol. Energy 268 (2024) 112256.

[27] S.S. Nair, P. Thakur, F. Wan, A. Trukhanov, L. Panina, A. Thakur, Performance evaluation and the optimization of an inverted photo-voltaic cell with lead-free double perovskite material and inorganic transport layer materials, Sol. Energy 262 (2023) 111823.

[28] S. Bimli, V. Manjunath, S.R. Mulani, A. Miglani, O.S. Game, R.S. Devan, Theoretical investigations of all inorganic Cs_2SnI_6 double perovskite solar cells for efficiency 30%, Sol. Energy 256 (2023) 76–87.

[29] M.A. Green, A. Ho-Baillie, H.J. Snaith, The emergence of perovskite solar cells, Nat. Photonics 8 (7) (2014) 506–514.

[30] S. Mahmud, M. Ali, M. Hossain, M. Uddin, DFT aided prediction of phase stability, optoelectronic and thermoelectric properties of A_2AuScX_6 (A=Cs, Rb; X=Cl, Br, I) double perovskites for energy harvesting technology, Vacuum 221 (2024) 112926.

[31] S. Mahmud, M. Hossain, M. Uddin, M. Ali, Prediction of X_2AuYZ_6 (X=Cs, Rb; Z=Cl, Br, I) double halide perovskites for photovoltaic and wasted heat management device applications, J. Phys. Chem. Solids 196 (2025) 112298.

[32] S. Mahmud, U. Ahmed, M.A.U.Z. Atik, M.M. Hossain, M.M. Uddin, M.A. Ali, Novel $Cs_2Au^IM^{III}F_6$ (M=As, Sb) double halide perovskites: sunlight and industrial waste heat management device applications, Phys. Chem. Chem. Phys. (2025).

[33] M.S. Uddin, M.K. Hossain, M.B. Uddin, G.F. Toki, M. Ouladsmane, M.H. Rubel, D.I. Tishkevich, P. Sasikumar, R. Haldhar, R. Pandey, An in-depth investigation of the combined optoelectronic and photovoltaic properties of lead-free $Cs_2AgBiBr_6$ double perovskite solar cells using DFT and SCAPS-1D frameworks, Adv. Electron. Mater. 10 (5) (2024) 2300751.

[34] S. Mushtaq, S. Tahir, A. Ashfaq, R.S. Bonilla, M. Haneef, R. Saeed, W. Ahmad, N. Amin, Performance optimization of lead-free $MASnBr_3$ based perovskite solar cells by SCAPS-1D device simulation, Sol. Energy 249 (2023) 401–413.

[35] M.S. Uddin, M.A. Al Mashud, G.I. Toki, R. Pandey, M. Zulfiqar, O. Saidani, K. Chandran, M. Ouladsmane, M.K. Hossain, Lead-free ge-based perovskite solar cell incorporating TiO_2 and Cu_2O charge transport layers harnessing over 25% efficiency, J. Opt. 53 (4) (2024) 3726–3742.

[36] S.M. Qaid, A. Shaker, K.D. Jayan, M. Alkadi, A.A.A. Ahmed, W. Zein, Design and numerical simulation of B-γ $CsSnI_3$-based perovskite solar cells: Conventional versus inverted configurations, Sol. Energy 268 (2024) 112275.

[37] C. Ming, H. Zhou, J. Wu, C. Hu, W. Fan, X. Ma, Z. Zeng, Y. Qi, J. Shi, S. Qiao, The design and performance optimization of all-inorganic $CsPbIBr_2/CsSnI_3$ heterojunction perovskite solar cells, Sol. Energy 263 (2023) 111885.

[38] M.K. Hossain, M.H.K. Rubel, G.I. Toki, I. Alam, M.F. Rahman, H. Bencherif, Effect of various electron and hole transport layers on the performance of $CsPbI_3$-based perovskite solar cells: a numerical investigation in DFT, SCAPS-1D, and wxAMPS frameworks, ACS Omega 7 (47) (2022) 43210–43230.

[39] A.A. Hossain, A. Khaleque, M.H. Galib, Eco-friendly $MASnI_3/CsSn_{0.5}Ge_{0.5}I_3$ based perovskite solar cell with interfacing layers for enhancing efficiency, Sol. Energy 278 (2024) 112763.

[40] M.H. Cho, H. Seol, A. Song, S. Choi, Y. Song, P.S. Yun, K.-B. Chung, J.U. Bae, K.-S. Park, J.K. Jeong, Comparative study on performance of IGZO transistors with sputtered and atomic layer deposited channel layer, IEEE Trans. Electron Devices 66 (4) (2019) 1783–1788.

[41] S. Chatterjee, A.J. Pal, Introducing Cu_2O thin films as a hole-transport layer in efficient planar perovskite solar cell structures, J. Phys. Chem. C 120 (3) (2016) 1428–1437.

[42] Y. Liu, J. Zhu, L. Cai, Z. Yao, C. Duan, Z. Zhao, C. Zhao, W. Mai, Solution-processed high-quality Cu_2O thin films as hole transport layers for pushing the conversion efficiency limit of Cu_2O/Si heterojunction solar cells, Sol. RRL 4 (1) (2020) 1900339.

[43] J. Jo, J.D. Lenef, K. Mashooq, O. Trejo, N.P. Dasgupta, R.L. Peterson, Causes of the difference between hall mobility and field-effect mobility for p-type RF sputtered Cu_2O thin-film transistors, IEEE Trans. Electron Devices 67 (12) (2020) 5557–5563.

[44] H.-H. Hsu, C.-Y. Chang, C.-H. Cheng, A flexible IGZO thin-film transistor with stacked TiO_2-based dielectrics fabricated at room temperature, IEEE Electron Device Lett. 34 (6) (2013) 768–770.

[45] K. Chakraborty, M.G. Choudhury, S. Paul, Study of physical, optical, and electrical properties of cesium titanium (IV)-based single halide perovskite solar cell, IEEE J. Photovoltaics 11 (2) (2021) 386–390.

[46] H. Liu, L. Xiang, Q. Liu, P. Gao, Y. Zhang, S. Li, F. Gao, Toward High-Performance HTL-Free All-Perovskite Tandem Solar Cells: SCAPS Simulation, IEEE J. Photovoltaics 14 (1) (2023) 59–64.

[47] A. Sunny, S. Rahman, M. Khatun, S.R.A. Ahmed, et al., Numerical study of high performance HTL-free $CH_3NH_3SnI_3$-based perovskite solar cell by SCAPS-1D, AIP Adv. 11 (6) (2021).

[48] S.M. Sze, Y. Li, K.K. Ng, Physics of Semiconductor Devices, John wiley & sons, 2021.

[49] Z. Zhang, Q. Sun, Y. Lu, F. Lu, X. Mu, S.-H. Wei, M. Sui, Hydrogenated $Cs_2AgBiBr_6$ for significantly improved efficiency of lead-free inorganic double perovskite solar cell, Nat. Commun. 13 (1) (2022) 3397.

[50] W. Xiang, E. Cronk, J. Wall, L. Li, K. Zhu, J.J. Berry, R.J. Lad, L. Yu, F. Yan, Double perovskite interlayer stabilized highly efficient perovskite solar cells, ACS Appl. Mater. Interfaces 16 (34) (2024) 44988–44996.

[51] K.I.F. Utsho, S. Mostafa, M. Tarekuzzaman, M.S. Al-Saleem, N.I. Nahid, J.Y. Al-Humaidi, M. Rasheduzzaman, M.M. Rahman, M.Z. Hasan, Optimizing $Cs_2CuBiBr_6$ double halide perovskite for solar applications: the role of electron transport layers in SCAPS-1D simulations, RSC Adv. 15 (3) (2025) 2184–2204.

[52] T.T. Ferdous, S.S. Urmi, M.A.K. Khan, M.A. Alim, Carrier transport layer engineering of $Cs_2TiI_2Br_4$ halide double perovskite solar cell via SCAPS 1D: Approaching the shockley-queisser limit, Micro Nanostructures 192 (2024) 207881.

[53] M.J. Hossen, M.B. Rahman, M.H. Miah, H.M. Hamzah, S.M. Said, S. Hatta, M.A. Islam, Modeling and optimization of high efficiency Pb-free Cs-based halide double perovskite solar cell using SCAPS-1D, J. Opt. (2025) 1–15.

[54] R. Yao, S. Ji, T. Zhou, C. Quan, W. Liu, X. Li, Self-energy correction and numerical simulation for efficient lead-free double perovskite solar cells, Phys. Chem. Chem. Phys. 26 (6) (2024) 5253–5261.

[55] M.K. Hossain, S. Islam, M.N. Sakib, M.S. Uddin, G.F. Toki, M.H. Rubel, J. Nasrin, S.H. Shahatha, M. Mohammad, A.A. Alothman, et al., Exploring the optoelectronic and photovoltaic characteristics of lead-free Cs_2TiBr_6 double perovskite solar cells: a DFT and SCAPS-1D investigations, Adv. Electron. Mater. 11 (2) (2025) 2400348.

[56] S.S. Dipta, M.A. Rahim, A. Uddin, Encapsulating perovskite solar cells for long-term stability and prevention of lead toxicity, Appl. Phys. Rev. 11 (2) (2024).

[57] Q. Wei, X. Huo, Q. Fu, T. Wang, H. Zhao, Y. Wang, J. Yang, S. Zhan, L. Zhou, S. Wang, et al., An effective encapsulation for perovskite solar cells based on building-integrated photovoltaics, J. Mater. Chem. C 10 (23) (2022) 8972–8978.